
This is an electronic reprint of the original article.
This reprint may differ from the original in pagination and typographic detail.

Wang, Yipeng; Haneda, Katsuyuki; Icheln, Clemens; Ala-Laurinaho, Juha; Tuomela, Juha; Vaha-Savo, Lauri; Xue, Bing; Chen, Xiaoming

Grating-Lobe Reduction for Uniform Under-Sampled Phased Array Using Dielectric Dome Lens

Published in:
IEEE Transactions on Antennas and Propagation

DOI:
[10.1109/TAP.2024.3508103](https://doi.org/10.1109/TAP.2024.3508103)

E-pub ahead of print: 01/01/2024

Document Version
Peer-reviewed accepted author manuscript, also known as Final accepted manuscript or Post-print

Please cite the original version:
Wang, Y., Haneda, K., Icheln, C., Ala-Laurinaho, J., Tuomela, J., Vaha-Savo, L., Xue, B., & Chen, X. (2024). Grating-Lobe Reduction for Uniform Under-Sampled Phased Array Using Dielectric Dome Lens. *IEEE Transactions on Antennas and Propagation*. Advance online publication. <https://doi.org/10.1109/TAP.2024.3508103>

This material is protected by copyright and other intellectual property rights, and duplication or sale of all or part of any of the repository collections is not permitted, except that material may be duplicated by you for your research use or educational purposes in electronic or print form. You must obtain permission for any other use. Electronic or print copies may not be offered, whether for sale or otherwise to anyone who is not an authorised user.

Grating-Lobe Reduction for Uniform Under-Sampled Phased Array Using Dielectric Dome Lens

Yipeng Wang, Katsuyuki Haneda, *Member, IEEE*, Clemens Icheln, Juha Ala-Laurinaho, Juha Tuomela, Lauri Vähä-Savo, *Member, IEEE*, Bing Xue, *Graduate Student Member, IEEE*, and Xiaoming Chen, *Senior Member, IEEE*

Abstract—Under-sampled arrays exhibit low mutual coupling, alleviating heat dissipation challenges associated with active radio frequency (RF) components in integrated front-end designs. This paper presents an effective dielectric dome lens (DDL) for a uniform array with one-wavelength inter-element spacing, enabling beam scanning with reduced grating lobes, making it suitable for millimeter-wave communication systems. The shape of the DDL is optimized using the geometric optics (GO) algorithm, allowing for the reflection of grating lobes while maintaining effective main beam scanning. The DDL is then miniaturized, integrated with absorber sheets to dissipate reflected grating lobes, and equipped with matching layers to improve radiation performance. The subsequent full-wave simulation further optimizes the design, accounting for factors overlooked by the GO algorithm and finalizing the DDL structure for operating with a under-sampled array. Finally, a 3×8 under-sampled rectangular patch array working at 28 GHz, integrated with a cylinder DDL, is fabricated and measured to validate the design approach. The experimental results are in agreement with the simulations. With the help of the DDL, the array with one-wavelength inter-element spacing achieves a continuous, symmetrical-to-boresight beam-scanning range of 110° , with a scan loss (SL) within 3 dB. The grating lobe is consistently reduced, maintaining peak side-lobe levels more than 9 dB below the main beam. This scanning performance remains effective over a bandwidth of 2 GHz.

Index Terms—Dielectric dome lens, under-sampled phased array, grating lobe reduction.

I. INTRODUCTION

THE multiple-input and multiple-output (MIMO) system is a crucial technology for fifth-generation (5G) and next-generation (6G) communications. It utilizes multiple antennas at both the transmitter and receiver to enhance communication performance through spatial multiplexing, diversity, and beam-forming. In beam-forming applications, a phased array that allows for flexible beam scanning is essential. This array is typically compact, with inter-element spacing of no more than $\lambda_0/2$, where λ_0 is the wavelength in free space at the operating frequency, to avoid grating lobes. However,

the mutual coupling should be carefully suppressed for the tightly coupled array to achieve the broad scanning range [1], [2], [3]. Nevertheless, a uniform under-sampled array with larger inter-element spacing, such as approximately λ_0 , offers several advantages. These include improved isolation, lower active reflection coefficients, and reduced spatial correlations in a multi-path environment with limited angular spread, all of which benefit the wireless communication system [4], [5]. Moreover, under-sampled arrays require fewer antenna elements and corresponding RF chains, which helps reduce hardware complexity, power consumption, and associated costs. Furthermore, as the frequency increases, heating becomes inescapable in the phased-array system. The narrow inter-element spacing is insufficient to support effective heat dissipation. Therefore, the uniform under-sampled array can potentially be at the core of a MIMO system, especially in a high-frequency band, as long as the grating lobes are well-reduced. Several works have been devoted to reducing grating lobes in the under-sampled array while maintaining good scanning performance. Some of them, based on the principle of the pattern multiplication [6], engineer far-field patterns of antenna elements to minimize the radiation toward the array-factor-associated grating lobe. Approaches include using pattern re-configurable antenna [7], [8], multi-mode antenna [9], [10], [11], [12], and replacing the original antenna element with a sub-array [13], [14], [15]. In addition, authors in [16], [17], [18], and [19] managed to reduce the grating lobe by optimizing the arrangement and excitation of antenna elements, resulting in an unequally spaced array with non-linear excitation amplitudes or phases. Nevertheless, the methods mentioned above typically require a special design on the antenna elements or the array, making it complex and non-flexible.

Some authors focus on designing structures near the uniform under-sampled array to reduce the grating lobes without affecting the array structure [20], [21], [22]. For instance, authors in [21] proposed a meta-grating design to reduce the grating lobe of a uniform under-sampled array consisting of line sources. Different from the traditional meta-surface, meta-grating has a relatively larger arrangement period (usually approximately one wavelength), capable of coupling energy from one propagation direction to another. With the array's broadside defined as 0° , a scanning range of $[60^\circ, 80^\circ]$ with a high energy coupling efficiency is achieved for the uniform

This research is partly sponsored by the China Scholarship Council (No. 202206280097). The authors from Aalto University acknowledge financial support from the Academy of Finland – NSF joint call pilot “Artificial intelligence and wireless communication technologies”, decision # 345178.

Y. Wang and X. Chen are with the School of Information and Communications Engineering, Xi'an Jiaotong University, Xi'an, 710049, China (e-mail: xiaoming.chen@mail.xjtu.edu.cn)

K. Haneda, C. Icheln, J. Ala-Laurinaho, J. Tuomela, L. Vähä-Savo, and B. Xue are with the School of Electrical Engineering, Aalto University, Espoo, 02150, Finland.

under-sampled array with an inter-element spacing of $0.93\lambda_0$. Moreover, when the main beam scans to 80° , the peak side-lobe level is about 5 dB below the main beam. Nevertheless, this work mainly focused on the semi-analytical design scheme and provided only simulated results, ignoring the coupling effects between the parasitic meta-grating and the line sources array. Furthermore, for an under-sampled array with an inter-element spacing of 0.96λ , the authors in [22] designed an angle-selective surface to reflect grating lobes, preventing them from reaching the far-field region. While the grating lobe is significantly reduced, the main beam scanning range remains limited to $\pm 15^\circ$, symmetrically centered around the broadside of the array. In addition, authors in [23] proposed a phase-gradient meta-dome combined with a phase pre-distortion method to enlarge the grating-lobe-free range of a phased array with an inter-element spacing of $0.6\lambda_0$. Nevertheless, this work only provides simulated results based on GO and physical optics, without mentioning the fabrication of the meta-dome and related measurement results.

Additionally, the DDL has been thoroughly investigated for its ability to enhance the scanning performance of the compact phased array, without considering the existence of grating lobes [24], [25], [26], [27]. Similar to the meta-surface [28], [29], the DDL is capable of affecting wave propagation by providing a desired insertion phase over the array's aperture [30]. However, the application of the meta-surface is limited by the high insertion loss and the high fabrication complexity induced by the tiny size of the periodic elements, especially in high frequencies. In contrast, the DDL can be easily fabricated using 3-D printing [24], [31], computer numerical control (CNC) machining [26], and injection molding with low-loss dielectric materials [32]. Nevertheless, the effectiveness of the DDL in enabling beam scanning for an under-sampled array, considering the presence of the grating lobe, has not yet been demonstrated.

This paper presents a DDL design methodology for a uniform under-sampled array with one-wavelength inter-element spacing, aiming at reduce grating lobes while enabling effective beam scanning. Theoretically, the initial shape of the DDL is obtained from a GO algorithm combined with an optimization process. The DDL's capability to reduce grating lobes is investigated through full-wave simulations in CST Studio Suite 2023. Additionally, a parameter sweep study based on the GO algorithm offers a comprehensive understanding of the DDL's scanning performance limitations. From theory to practice, the DDL is miniaturized, integrated with absorber sheets to dissipate reflected grating lobes, and equipped with matching layers to improve radiation performance. Furthermore, another optimization process based on the full-wave simulation is applied to better evaluate the array's radiation performance, considering the near-field effect, antenna couplings, multiple reflections, and material loss. Finally, a 3×8 under-sampled rectangular patch array and a cylinder DDL are designed, fabricated, and measured at 28 GHz. The measured results agree with the simulations, demonstrating the effectiveness of the DDL design method. The radiation performance of the antenna elements and the scanning performance of the under-sampled array integrated with the cylinder DDL are also

investigated and discussed.

II. PERFORMANCE METRICS

To provide background on the method, definitions of the coordinate system and scanning performance metrics for under-sampled arrays will be reviewed prior to presenting the detailed DDL design method.

A. Coordinate System

In this paper, the XYZ coordinate system is defined as shown in Fig. 1(a). The azimuth angle ϕ ranges from 0° to 360° , starting from the positive direction of the x -axis, while the elevation angle θ spans 0° to 180° , beginning from the positive z -axis. The linear and planar arrays are arranged on the yz plane and are oriented to radiate towards the positive x -direction ($x > 0$). In addition, the linearly polarized antennas are oriented so that the xoy plane ($\theta = 90^\circ$) corresponds to the H-plane, while the E-plane denotes the xoz plane ($\phi = 0^\circ$).

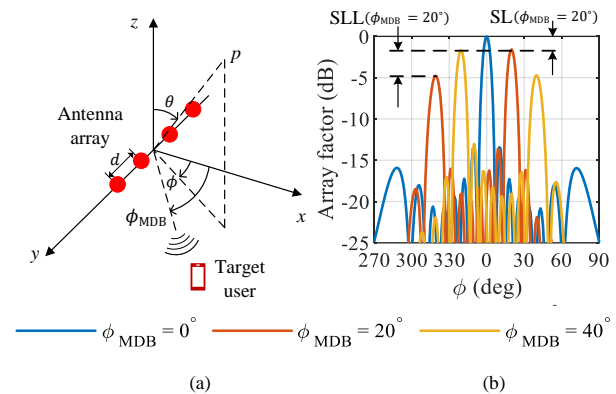


Fig. 1. (a) Global XYZ coordinate system, antenna array, and target user. (b) Illustrations of scan loss (SL) and side-lobe level (SLL) of the array with one-wavelength inter-element spacing ($d = \lambda$).

B. Scanning Performance Metrics for Under-Sampled Arrays

For the array with an inter-element spacing of one wavelength, the main direction beam (MDB) is defined as the beam directed towards the target angle, denoted by $\phi = \phi_{MDB}$ on the H-plane, as illustrated in Fig. 1(a). The gain variation observed as the MDB scans from broadside ($\phi = 0^\circ$) to other directions is termed scan loss (SL) and is measured in dB. Additionally, the ratio between the MDB and the peak amplitude of the side-lobes defines the side-lobe level (SLL), as shown in Fig. 1(b). When the MDB is oriented at angle ϕ_{MDB} , the array's radiation pattern on the xoy plane, as a function of ϕ , is represented as $G(\phi, \phi_{MDB})$ in dB. If the strongest side-lobe occurs at $\phi = \phi_{SL}$, the equations for SL and SLL can be expressed as

$$\begin{aligned} \text{SL}(\phi_{MDB}) &= G(\phi = 0, \phi_{MDB}) - \\ &G(\phi = \phi_{MDB}, \phi_{MDB}), \\ \text{SLL}(\phi_{MDB}) &= G(\phi = \phi_{MDB}, \phi_{MDB}) - \\ &G(\phi = \phi_{SL}, \phi_{MDB}) \end{aligned} \quad (1)$$

For the radiation pattern with $\phi_{\text{MDB}} = 20^\circ$, the gain of the MDB is typically higher than that of the grating lobe at $\phi = 318^\circ$, resulting in a positive SLL, as shown in Fig. 1(b). However, it is important to note that the amplitude of the side-lobe peak can occasionally exceed that of the MDB, leading to a negative SLL. This is demonstrated in the radiation pattern for $\phi_{\text{MDB}} = 40^\circ$ in Fig. 1(b), where the gain of the grating lobe, located at approximately 340° , surpasses that of the MDB.

In [23] and [26], the authors proposed a method to increase the scan range of an array with an inter-element spacing of $d = 0.6\lambda_0$ while avoiding the grating lobe. Specifically, they limit the main beam of the standalone array to the grating-lobe-free region, $\phi_{\text{MDB}}^{\text{Array}} \subseteq [0^\circ, 40^\circ]$, and design a DDL or a phase-gradient meta-dome to deflect the main beam, thereby covering angles beyond 40° , as shown in Fig. 2(a). However, as shown in Fig. 2(b), for a uniform phased array with an inter-element spacing of $d = \lambda_0$, this method becomes ineffective, as the grating lobe consistently exists within the field of view (FOV), defined as $\phi \subseteq [270^\circ, 360^\circ] \cup [0^\circ, 90^\circ]$, even when the main beam is directed at broadside ($\phi_{\text{MDB}} = 0^\circ$).

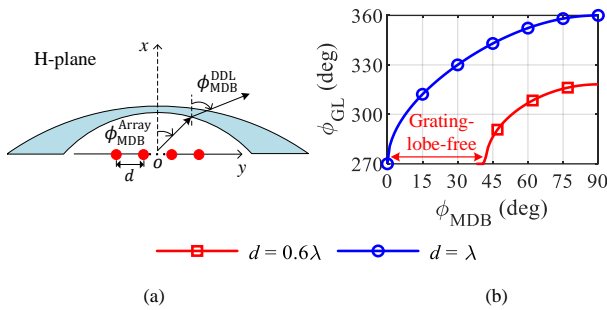


Fig. 2. (a) Expansion of scan region using a DDL. (b) Locations of the array's main direction beam (MDB) and grating lobe (GL) for different inter-element spacings, d .

To address the unavoidable presence of grating lobes, we adopt an optimization approach in the DDL design to deflect these lobes outside the FOV and subsequently dissipate them. For this electrically large-scale problem, the GO algorithm is employed to efficiently evaluate the radiation pattern when the under-sampled array is integrated with the DDL. Additionally, full-wave simulation is applied to evaluate the electric field distribution within the structure, providing insight into the mechanisms behind grating lobe reduction through the DDL. This simulation also play an important role in further optimizing and finalizing the prototype of the array integrated with the DDL. Fig. 3 presents a flowchart outlining the steps of the DDL design process.

III. APPLICATION OF THE GO ALGORITHM IN ARRAY WITH DDL

A. Simplified Model for GO Algorithm: Array with DDL

A simplified model of the array equipped with the DDL is established for the GO algorithm and further optimization, as shown in Fig. 4(a). The beam scanning performance on the xy plane will be investigated. In practical applications, this

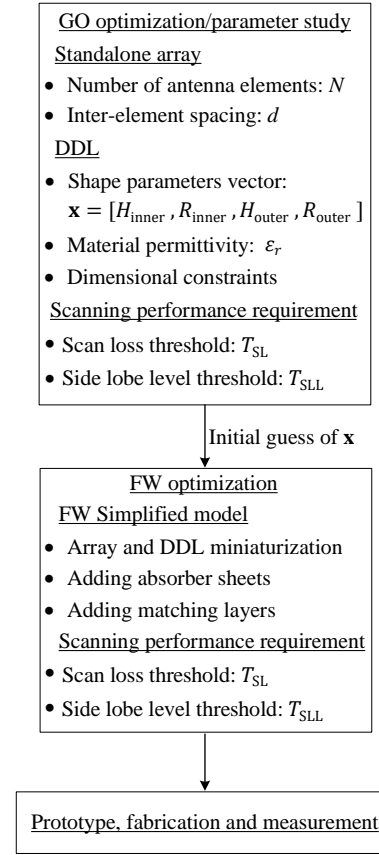


Fig. 3. Flowchart of the DDL design process for the under-sampled array.

can be readily achieved using a cylindrical lens, which offers the advantage of straightforward fabrication. Accordingly, the DDL is assumed to be infinite in the z -direction, and Fig. 4(a) depicts its cross-section on the xy plane. Moreover, as shown in Fig. 4(a), a uniform under-sampled array with N ideal point sources is positioned along the y -axis. Two assumptions are made applicable to this model:

1) On the xy plane, for simplicity, the inner $r_{\text{inner}}(\phi)$ and outer contour $r_{\text{outer}}(\phi)$ of the DDL are part of circles centering on the x -axis at $(-(R_{\text{inner}} - H_{\text{inner}}), 0, 0)$, and $(-(R_{\text{outer}} - H_{\text{outer}}), 0, 0)$, respectively. $R_{\text{inner/outer}}$ and $H_{\text{inner/outer}}$ are the radius and height of the inner/outer contour, respectively. On the xy plane, the contour $r(\phi)$ can be represented using its radius R and height H as

$$r(\phi) = \sqrt{R^2 - (R - H)^2 \cdot \sin^2(\phi)} - (R - H) \cdot \cos(\phi), \quad (2)$$

in which $\phi \subseteq [270^\circ, 360^\circ] \cup [0^\circ, 90^\circ]$.

2) The uniform under-sampled array consists of N ideal point sources with an inter-element spacing of d . N_{Ray} rays radiated by each antenna element reaching the observation curve with a radius of $R_{\text{far-field}}$ will be recorded as the far-field (2D) radiation pattern. The electric field \mathbf{E} of each ray has two components, parallel and perpendicular with respect to the xy plane, E_{\perp} and E_{\parallel} , as shown in Fig. 4(a). For simplicity, each antenna element radiates only within the region $x > 0$, with back-lobes not considered.

4) *Variation of the Electric Field and Curvature Matrix in the Uniform Medium:* When the ray travels in free space or within the DDL structure, the variations in the curvature matrix, \mathbf{Q} , and the field intensity, u , along the ray path from position \mathbf{r}_0 to \mathbf{r}_1 can be expressed as [33]

$$\mathbf{Q}^{-1}(\mathbf{r}_1) = \mathbf{Q}^{-1}(\mathbf{r}_0) + \|\mathbf{r}_1 - \mathbf{r}_0\| \begin{bmatrix} 1 & 0 \\ 0 & 1 \end{bmatrix}, \quad (8a)$$

$$u(\mathbf{r}_1) = u(\mathbf{r}_0) \left[\frac{\det(\mathbf{Q}(\mathbf{r}_1))}{\det(\mathbf{Q}(\mathbf{r}_0))} \right]^{1/2} \exp(-jk \|\mathbf{r}_1 - \mathbf{r}_0\|) \quad (8b)$$

where k is the wave number of the uniform medium.

IV. DDL SHAPE OPTIMIZATION AND PERFORMANCE ANALYSIS

A. Array Synthesis and Objective Function

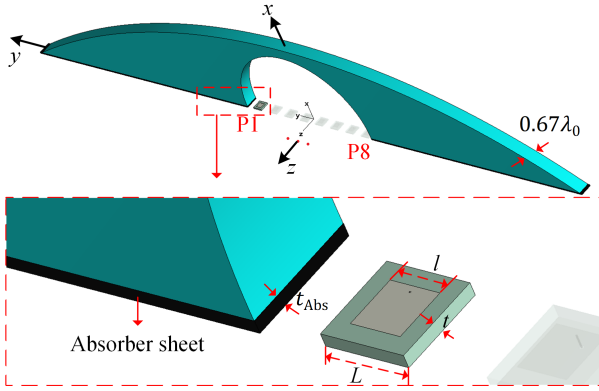


Fig. 5. Full-wave simulation model for validating the DDL dimension estimates derived from the GO algorithm, in which periodic boundary conditions are set in the z -direction. The dimensions of the patch antenna and absorber sheet are $l = 3.21$, $L = 5.36$, $t = 0.787$, and $t_{Abs} = 0.8$ (units: mm).

For the given DDL defined by the shape parameter vector $\mathbf{x} = [H_{inner}, R_{inner}, H_{outer}, R_{outer}]$, the 2D radiation pattern for the n -th (where $n = 1, \dots, N$) antenna element in the array is denoted as $G_n(\mathbf{x}, \phi)$, where ϕ is in the range $[270^\circ, 360^\circ] \cup [0^\circ, 90^\circ]$. Therefore, for the target user at $\phi = \phi_{MDB}$, the radiation pattern of the array integrated with the DDL, denoted as $G_{array}(\mathbf{x}, \phi, \phi_{MDB})$, and the excitation phase of the n -th antenna element, $\beta_n(\phi_{MDB})$, can be represented as

$$G_{array}(\mathbf{x}, \phi, \phi_{MDB}) = \sum_{n=1}^N e^{j\beta_n(\phi_{MDB})} \cdot G_n(\mathbf{x}, \phi), \quad (9a)$$

$$\beta_n(\phi_{MDB}) = -L G_n(\mathbf{x}, \phi = \phi_{MDB}) \quad (9b)$$

The excitation phases of the antenna elements, derived from (9b), align the phases of the antenna radiation patterns in the target direction, thereby achieving maximum MDB gain. Moreover, the behavior of the grating lobe associated with these excitation phases depends on DDL's shape parameter vector \mathbf{x} , which will be optimized. Consequently, once the vector $\mathbf{x} = [H_{inner}, R_{inner}, H_{outer}, R_{outer}]$ is determined, the array's radiation patterns $G_{array}(\mathbf{x}, \phi, \phi_{MDB})$, and the associated SL and SLL, can be determined for various ϕ_{MDB} values.

Furthermore, given that the selection choices of DDL materials is often limited or typically predetermined, the optimization process primarily aims to identify the appropriate vector \mathbf{x} that effectively reduces the grating lobe while maintaining an acceptable SL. Taking into account the definitions of SL and SLL presented in (1), the optimization problem can be formulated as

$$\begin{aligned} & \max_{\mathbf{x}} |\phi_{MDB}| \\ & \text{s.t.} \\ & \left\{ \begin{array}{l} \text{SL}(\phi) \leq T_{SL} \text{ (dB)}, \quad \phi \in [0^\circ, \phi_{MDB}], \\ \text{SLL}(\phi) \geq T_{SLL} \text{ (dB)}, \quad \phi \in [0^\circ, \phi_{MDB}] \end{array} \right. \end{aligned} \quad (10)$$

where T_{SL} and T_{SLL} represent the thresholds of the SL and the SLL, respectively. Furthermore, in this paper, the Surrogate Optimization integrated into Matlab [36], suitable for expensive objective functions with bounds and optional integer constraints, is chosen to solve (10).

B. Optimization Results and Performance Analysis

In this subsection, the GO algorithm and the optimization (10) are applied to a standalone antenna array to evaluate the performance of reducing the grating lobe using a DDL. The standalone array, working at 28 GHz, has $N = 8$ E_{\perp} -polarized antenna elements with an inter-elements spacing of λ_0 . It should be noted that the optimization (10) is also suitable for E_{\parallel} -polarized antennas. For each antenna element, 1000 rays are generated uniformly within its FOV. The rays have the same amplitude and phase distribution as the complex far-field radiation pattern of the patch antenna, whose substrate has a permittivity of $\epsilon_r = 2.2$, and dimensions are summarized in Fig. 5. The lossless DDL's relative permittivity ϵ_r is 4.3. In practice, the values of T_{SL} and T_{SLL} in (10) can be adjusted according to specific applications. In this paper, as one possible case, T_{SL} and T_{SLL} are set to 3 dB and 9 dB, respectively. This is based on the SLL values of 9.3 dB and 8.4 dB for phased arrays with inter-element spacing of approximately 0.9λ , as reported in references [7] and [37].

Moreover, in optimization, H_{outer} is set within $[\lambda_0, 5\lambda_0]$ for a low-enough profile. It should be noted that, the upper bound of H_{outer} can be selected according to practical requirements, while the lower bound ensures sufficient distance to ensure the effectiveness of the GO algorithm. H_{inner} is then set within $[\lambda_0, H_{outer})$. In addition, the radius of the two contours of the DDL has the limitation of $(R_{outer}, R_{inner}) \subseteq [4\lambda_0, 200\lambda_0]$, in which the lower bound is according to the minimum value that the DDL will not intersect with the antenna array and the upper bound is set to make the contour almost flat over the array.

1) *Optimization Results and Validation:* Fig. 6(a) depicts the scanning performance of one case resulting from optimization, which has a scan region of $\phi_{MDB} \subseteq [304^\circ, 360^\circ] \cup [0^\circ, 56^\circ]$ because of the structure symmetry. The shape parameters of the DDL are $H_{inner} = 45.33$, $R_{inner} = 43.38$, $H_{outer} = 51.57$ and $R_{outer} = 374.56$ (unit: mm). With the DDL, the side-lobe of the standalone array is more than 9 dB lower than the MDB while maintaining an SL of less than 3 dB.

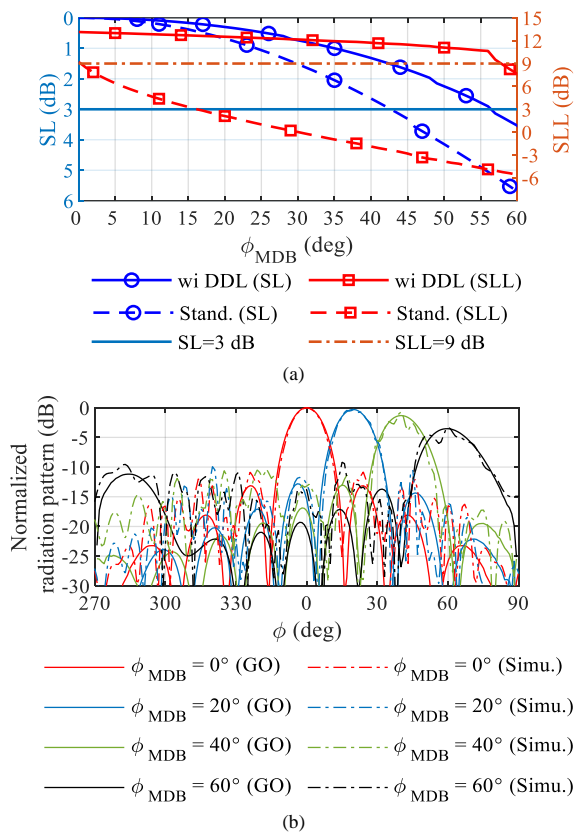


Fig. 6. (a) The scan loss (SL) and side-lobe level (SLL) of the standalone array and the array with DDL from the GO optimization. (b) Normalized far-field radiation patterns of the array with DDL at different scan angles $\phi_{MDB} = 0^\circ, 20^\circ, 40^\circ$, and 60° .

A full-wave simulation is performed to demonstrate the GO algorithm's effectiveness and find mechanisms behind the reduction of the grating lobe of the standalone array, as shown in Fig. 5. The periodic boundary condition is defined on two xy planes at $z = \pm 0.335\lambda_0$ to mimic an array along z -axes that are repeating infinitely with an inter-element spacing of $0.67\lambda_0$. This spacing represents a representative value for the vertical inter-element distance in a real base station [38], enabling an extremely narrow beamwidth in the xoz plane. This value is also utilized in the design of the 3×8 patch array, which will be described in detail in Sec. VI. Moreover, for the observation simplicity, an absorber sheet with a return loss of -23 dB at 28 GHz is attached to the bottom of the DDL at $x = 0$ to minimize the effects of the multiple reflections on the electric field distribution near the DDL and the far-field radiation pattern of the array with DDL. In addition, the antenna elements' far-field radiation patterns on the xy plane are simulated sequentially by placing the patch antenna at P1 to P8 and then interpolated and synthesized to calculate the array's pattern referring to (9a), and the results are shown in Fig. 6(b). Although some distortions caused by multiple reflections between the inner and outer contours appear in the full-wave simulated patterns, an agreement is found on the gain and shape of the patterns, proving the GO algorithm's effectiveness in the DDL design. It should be noted that the near-field effects such as the coupling between the antennas,

DDL material loss, and the multiple reflections between the outer/inner contour and the ground plane of the patch array are not taken into consideration in the GO algorithm. However, these effects can be adequately addressed in a subsequent optimization process within the full-wave simulation, which is based on the initial design derived from the GO optimization. This process will be discussed in Section V.

2) *Performance Analysis:* In the full-wave simulation, the electric field magnitude, i.e., \mathbf{E}_\perp distribution, on the xy plane can be obtained by exciting the patch antennas with the DDL simultaneously, and the result is shown in Fig. 7(a). The figure corresponds to excitation phases for $\phi_{MDB} = 45^\circ$ that are calculated using (9a) and the electric field distribution of the standalone array, as shown in Fig. 7(b), corresponding to the same excitation phases. According to Fig. 7, two main functions of the DDL can be found: the DDL 1) deflects the MDB from 27° to 45° and 2) reflects the grating lobe. Therefore, the total reflection critical angle [35] at the outer contour plays an essential role in the grating lobe reduction. Moreover, when the MDB continually scans over 56° range, the gain of the MDB decreases; meanwhile, the grating lobe's total reflection also starts to weaken, resulting in the SLL decreasing quicker when $\phi_{MDB} > 56^\circ$, as shown in the red solid curve with the square mark in Fig. 6(a).

Since the DDL is a structure that inevitably increases the profile of the phased-array, the scanning performance regarding the DDL material's permittivity and profile, i.e., H_{outer} , is worth evaluating. Therefore, the scanning performance subject to the constraints as $T_{SL} = 3$ dB and $T_{SLL} = 9$ dB of the DDL with different permittivity ϵ_r and H_{outer} is investigated by sweeping the other shape parameter combinations ($H_{inner}, R_{inner}, R_{outer}$) in the ranges $H_{inner} \subseteq [\lambda_0, H_{outer})$ and $(R_{outer}, R_{inner}) \subseteq [4\lambda_0, 200\lambda_0]$; they were swept across 35, 800 and 200 possible values respectively, each giving $\max(\phi_{MDB})$ fulfilling (10). Their empirical cumulative distribution functions (CDFs) are shown in Fig. 8, indicating that the higher ϵ_r and H_{outer} allows larger maximum scan angle of the array with DDL. Nevertheless, a lower permittivity (e.g., $\epsilon_r = 2.2$) can also be chosen for a better gain without considering the matching layers' design due to the weak reflection when the maximum scan angle criteria are not strict, e.g., $\max(\phi_{MDB}) = 30^\circ$. Furthermore, as illustrated in Fig. 8(b), increasing the SLL threshold T_{SLL} from 9 dB to 11 dB leads to a reduction in the maximum achievable scan angle of the array with DDL, decreasing from 49° to 46° . This indicates a trade-off between T_{SLL} and the maximum scan angle.

Although the GO algorithm applied to the simplified model depicted in Fig. 4(a) demonstrates greater efficiency compared to the full-wave simulation, it still requires approximately four days of parallel computing in MATLAB [39] on a personal computer (PC) equipped with an Intel-14700KF CPU and 128 GB of RAM to perform a comprehensive parameter sweep over all possible combinations of the shape parameter vector \mathbf{x} , resulting in one curve shown in Fig. 8(a). Consequently, conducting a preliminary parameter sweep with approximately one hundred combinations, followed by selecting \mathbf{x} that maximizes the scan angle while satisfying the two constraints specified in (10) as the starting point for the

subsequent GO optimization process, can significantly enhance the efficiency of the optimization. This approach takes about three hours on the same PC to obtain the optimal \mathbf{x} , enabling the array with the DDL to achieve the same maximum scan angle as the result derived from the comprehensive parameter sweep. Nevertheless, considering the material and dimensional constraints of the DDL, as well as the T_{SL} and T_{SLL} in accordance with the application requirements, performing a parameter sweep remains valuable for investigating limitations on scanning performance when necessary.

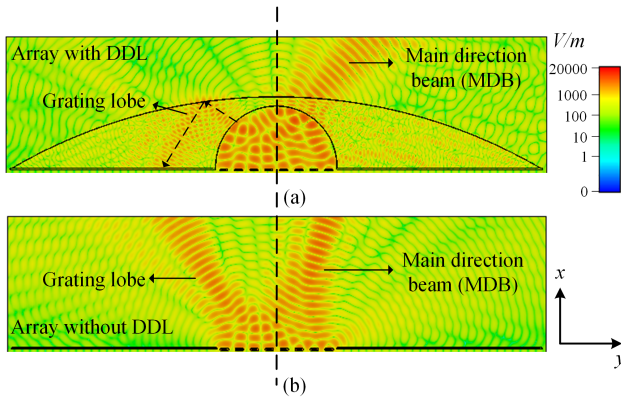


Fig. 7. Full-wave simulated electric field magnitude distributions of the array (a) with and (b) without the DDL.

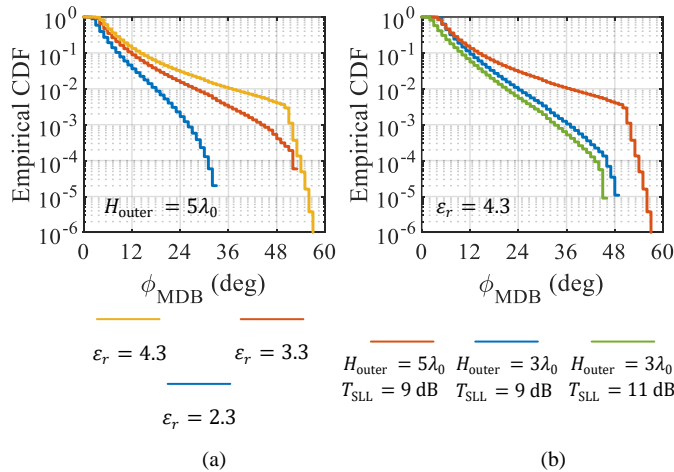


Fig. 8. CDF of the maximum scan angle ϕ_{MDB} of (a) the DDL with different permittivity when $H_{outer} = 5\lambda_0$, and (b) the DDL with different H_{outer} and T_{SLL} when $\epsilon_r = 4.3$.

V. DESIGN OF PATCH ARRAY EQUIPPED WITH DDL

The GO algorithm and the optimization process used in Sec. IV can quickly investigate the scanning performance of the array with the DDL, and give an initial design of the DDL according to the dimensional requirements. Nevertheless, When making this design from theory to practice, structural updates to the DDL are necessary. Therefore, further optimization based on the full-wave simulation is required to account for all the structural changes and details ignored by the GO algorithm.

The simplified model for full-wave simulated optimization is shown in Fig. 9(e), which has the same boundary conditions as indicated in Fig. 5. The periodic boundary condition enables efficient analysis of scanning performance on the xoy plane when the array repeats periodically and infinitely along the z -direction. Moreover, examining the scanning performance on a single plane with periodic boundaries enables the extension to two-dimensional beam scanning for a uniform square planar array by applying the principle of rotational symmetry [24]. Additionally, Fig. 9(e) illustrates several modifications to the DDL structure, and the design methods and their effects on beam scanning performance will be discussed in detail later.

As shown in Fig. 9(d), the standalone array consists of eight patch antennas working at 28 GHz, with a -10 dB matching bandwidth of 2 GHz. The inter-element spacing is λ_0 at the center frequency. The substrate cube of each patch antenna has a relative permittivity of 2.2 and a thickness of 0.787 mm. These patch antennas are embedded in the metal board to avoid antenna couplings. Furthermore, the chosen material for the DDL is PPE430 [32], manufactured by Avient. This material has a relative permittivity of 4.3 and an approximate loss tangent $\tan \delta$ of 0.0025 over 25 to 35 GHz.

In the optimization of the model shown in Fig. 9(e), the objective function, optimization vector \mathbf{x} , and the two constraints involving T_{SL} and T_{SLL} are identical to those defined in (10). Moreover, the DDL shape parameter vector \mathbf{x} derived from the GO-optimization serves as the start point. Notably, the far-field radiation patterns of the patch array integrated with the DDL are calculated using the full-wave simulation, considering all the details such as near-field effects, multiple reflections, material loss, antenna couplings, and structural modifications to the DDL.

The optimized shape parameters of the simplified model from the full-wave simulations are $H_{inner} = 43.91$, $R_{inner} = 44.38$, $H_{outer} = 46.79$ and $R_{outer} = 1370.20$ (unit: mm). As shown in Fig. 10(a), the realized scanning performance is better than the one optimized by GO without the full-wave simulation, achieving an SLL larger than 9 dB over the entire MDB angle range, i.e., $\phi_{MDB} \leq 56^\circ$. Additionally, although the DDL shape parameter vector \mathbf{x} remains the same, the solid SL and SLL curves in Fig. 6(a), derived from the ideal GO simplified model in Fig. 4(a), are smoother than the dashed SL and SLL curves in Fig. 10(a), which are derived from the full-wave simplified model depicted in Fig. 9(e). The oscillations observed in the dashed SL and SLL curves in Fig. 10(a) result from the realistic conditions included in the full-wave simplified model, such as multi-reflections, matching layer implementation, material losses, and antenna couplings. However, the scanning performance degradation caused by those realistic conditions can be effectively mitigated by complementing the GO-optimization process with further full-wave-simulated optimization.

Consequently, the main steps to build the simplified model, shown in Fig. 9(e), based on the initial design from the GO optimization, are as follows:

1) Uniform under-sampled array and DDL miniaturization:

Since only a portion of the DDL accounts for the MDB deflection and the grating lobe reflection, as shown in Fig. 7(a),

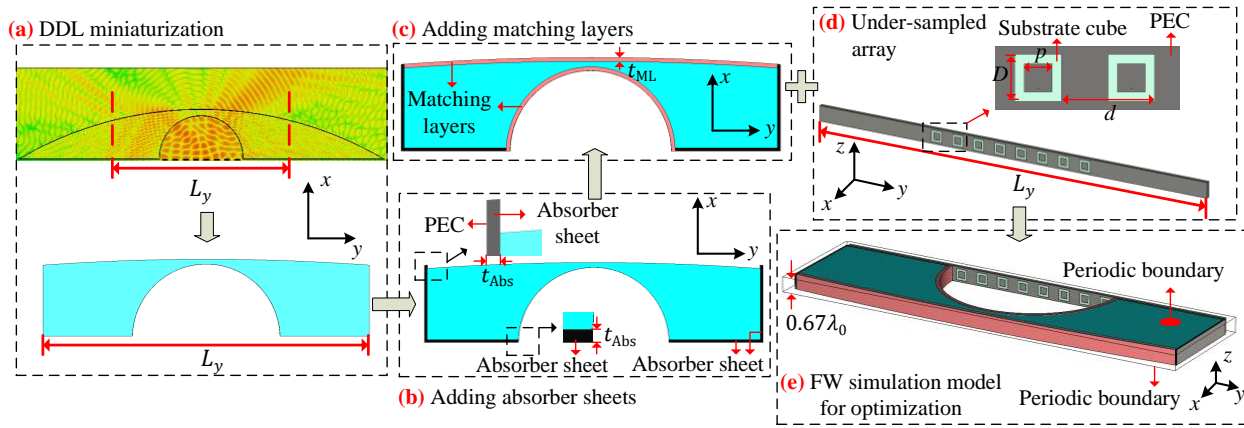


Fig. 9. Steps (a) - (d) to build the full-wave (FW) simulation model (e) for optimization, in which $L_y = 196$, $t_{Abs} = 0.8$, $t_{ML} = 2$, $p = 3.21$, $d = 10.71$, and $D = 5.36$ (units: mm).

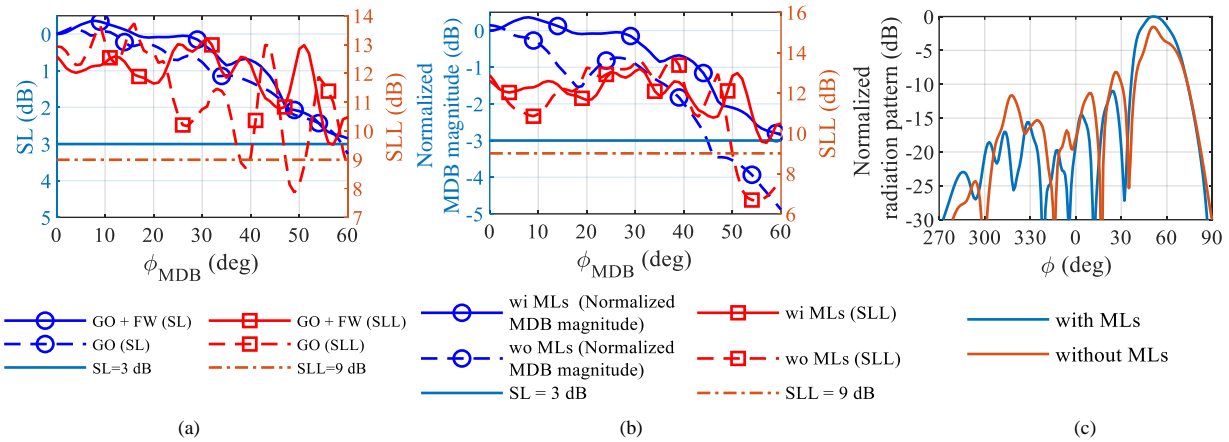


Fig. 10. (a) Scan loss (SL) and side-lobe level (SLL) of array integrated with DDL, using shape parameter vector \mathbf{x} from GO-optimization alone and from GO-optimization with additional full-wave-simulated (FW) optimization. (b) Scan loss (SL) and side-lobe level (SLL) of array integrated with DDL, with and without matching layers (MLs). (c) Simulated radiation patterns for $\phi_{MDB} = 55^\circ$ on the xoy plane of array integrated with DDL, with and without matching layers (MLs).

the DDL can be miniaturized by cutting some uninfluential portion according to the electric field distribution of the MDB and the grating lobe. The length of the DDL is $L_y = 196$ mm, as shown in Fig. 9(a).

2) *Adding absorber sheets*: The grating lobe reflected by the outer contour of the DDL should be appropriately dissipated. Otherwise, it would radiate towards the far-field region after bouncing many times and finally deform the array's far-field pattern, as shown in Fig. 11. Therefore, the absorber sheet manufactured by Atlantic Microwave [40], having a thickness t_{Abs} of 0.8 mm and a return-loss larger than 20 dB over 27 - 29 GHz, is used to dissipate the reflected grating lobe, as shown in Fig. 9(b). It should be noted that extra PEC sheets should be added to the outer surface of the side-absorber sheets to achieve a good absorption [40]. With the help of the absorber sheets, the far-field radiation pattern of the array with DDL becomes smoother, and the side-lobe also decreases due to suppressed multiple reflections, as shown in Fig. 11(c). It should be noted that in the state-of-art studies [23] [24] [26], DDLs are designed solely to deflect the main beam in compact arrays, without consideration of the presence of

grating lobes. In contrast, our approach involves a standalone array with an inter-element spacing of one wavelength, which inherently lacks a grating-lobe-free region, as illustrated in Fig. 2(b). Consequently, the dual objectives of deflecting the MDB and reflecting grating lobes to mitigate interference necessitate a compromise in the DDL design. This underscores the need to address multi-reflections caused by both reflected grating lobes and the partially efficient MDB, and to explore additional solutions to mitigate their effects on the far-field radiation patterns. Therefore, the need for a dissipation method in our research – specifically, the use of absorber sheets – is not to compensate for an inadequately optimized DDL. Instead, it addresses a previously unexplored issue: enabling beam scanning for an under-sampled array through DDL while accounting for the presence of grating lobes.

3) *Adding matching layers*: Matching layers are necessary for the DDL of high-permittivity material to reduce the reflections at the air-dielectric interfaces, resulting in a high transmission coefficient and desired gain. There are two different methods for the matching-layer design: adding holes to the DDL surface [24] and a $\lambda/4$ -thick dielectric layers [26]

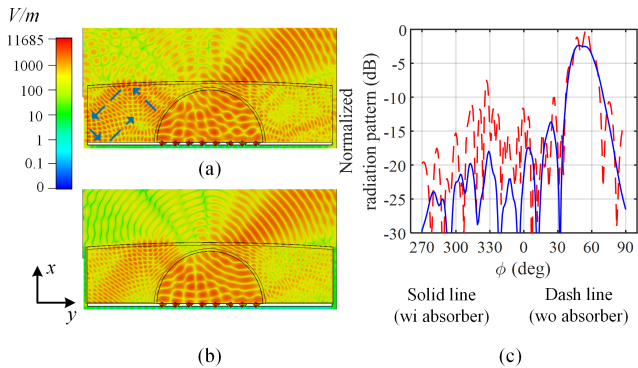


Fig. 11. Comparison of the simulated electric field magnitude distribution on the xy plane of array equipped with DDL: (a) without absorber sheets and (b) with absorber sheets. (c) Comparison of simulated far-field radiation patterns on the xy plane of the array equipped with DDL, with and without absorber sheets.

[27]. In this paper, the latter is chosen for the convenience of fabricating and assembling. In the simplified model, PTFE sheets are selected to be the inner and the outer matching layers of the DDL, as shown in Fig. 9(c). It has a $\epsilon_{ML} \approx 2.1$ that is close to the desired value $\epsilon_{ML}^{des} = \sqrt{\epsilon_{lens}} \approx 2.07$, and a thickness of 2 mm approximately to the desired value of $t_{ML} = (\lambda_0/\sqrt{\epsilon_{ML}})/4 = 1.85$ mm. The scanning performance shown in Fig. 10(b) indicates the matching layers can significantly increase the gain of the array with DDL, without influencing the SLL except for $\phi_{MDB} \subseteq [50^\circ, 60^\circ]$. Moreover, the radiation patterns for $\phi_{MDB} = 55^\circ$, as depicted in Fig. 10(c), indicate that the decrease in the gain of MDB and the increase in the side-lobe level collectively contribute to the observed decrease in the SLL shown in Fig. 10(b). Nevertheless, the full-wave simulated optimization can ensure that the scanning performance fulfills the two constraints defined in (10) over the whole scan range.

VI. EXPERIMENTAL DEMONSTRATION

A. Descriptions of Fabrication and Experiments

In this section, a 3×8 vertically (\mathbf{E}_\perp) polarized uniform under-sampled patch antenna array with DDL is simulated, prototyped, and the experimental performance is compared against the simulated ones to demonstrate the effectiveness of the proposed design method. The uniform under-sampled array with DDL works at 28 GHz with a -10 -dB operation bandwidth from 27 - 29 GHz, and the simulated structure is shown in Fig. 12. As seen from Fig. 12(c), the three antenna elements in the same column with an inter-element spacing of 0.67λ are synthesized with the same excitation magnitude and phases to achieve a vertically narrow beam radiating to bore-sight [38]. Then, the eight three-element subarrays are phased again to perform scanning on the horizontal plane. The substrate of the patch array is made of Arlon 880 with $\epsilon_r = 2.2$, $\tan \delta = 0.002$, and a thickness of 0.787 mm. Furthermore, patch antennas are surrounded by metal vias connecting to the upper and bottom metal ground to reduce the mutual coupling between antennas. In addition, the DDL, matching layers, absorber sheets, and patch array are assembled with

plastic screws, as shown in Fig. 12(a) - (b). Note that the z-directional thickness of the DDL should be sufficient to cover all twenty-four patch antennas, with additional space reserved for screw holes and assembly structures. The main shape parameters (i.e., $H_{inner/outer}$ and $R_{inner/outer}$) of the DDL, thickness of matching layers and absorber sheets are all the same as the optimized results using full-wave simulation in the Sec. V. Their dimensions are summarized in Figs. 9 and 12.

The fabricated patch array and the DDL are shown in Fig. 13(a) - (c). Each antenna element is fed with a semi-rigid coaxial cable length of about 15 cm, and a foam fixture is used to keep all the cables stable. Moreover, several plastic fixtures are designed to support the array with the test equipment. During the test, radiation patterns of each of the 24 patch antennas, within the scope of $\theta \subseteq [0^\circ, 180^\circ]$ and $\phi \subseteq [270^\circ, 360^\circ) \cup [0^\circ, 90^\circ)$, i.e., the front half sphere including magnitude and phase, are measured in the anechoic chamber, as shown in Fig. 13(d). When performing a test on one port, the rest of the ports are all matched with loads.

B. Element Patterns, Efficiency, and Reflection Coefficients

Fig. 14 shows several simulated and measured embedded antenna radiation patterns, which are in agreement in both E- and H-planes. Nevertheless, the multiple reflections between the inner and outer contour of the DDL cause fluctuations in the element patterns, as shown in Fig. 14(a)-(b) and (d)-(e). The reflection coefficients measured from elements No. 3 and No. 11 in the patch array are not influenced by the DDL, maintaining levels below -10 dB from 27 - 29 GHz, as shown in Fig. 14(f). This indicates that the multiple reflections caused by the DDL have a minimal effect on the patch antennas, while those in areas covered by the absorber sheets will be dissipated. Additionally, the measured coupling between elements No. 11 and No. 12 is lower than -25 dB from 27 - 29 GHz, and even below -35 dB between elements No. 12 and No. 15 due to the one wavelength horizontal inter-element spacing.

Moreover, for most of the antenna elements in the array with DDL, the simulated and measured half sphere antenna efficiencies are in good agreement, as shown in Fig. 14(c). In addition, the simulated total sphere antenna efficiencies are closer to the half sphere ones, indicating that for each element in the array with DDL, less power leaks backward and contributes to back lobes. Furthermore, compared to the standalone array, the DDL significantly affects the edge elements (e.g., element No. 2 in the array), resulting in their lower realized gain (Fig. 14(a) and (d)) and lower efficiency (Fig. 14(c)) than other elements in the middle of the array (e.g., element No. 13 in the array). Indeed, the DDL reduced the antenna efficiency of elements in the array. However, without investigating the array's scanning performance, it is difficult to evaluate the impact of the reduction in antenna efficiency on specific directions, such as the target direction and the direction of the grating lobes, which are regarded as interference for the radio service.

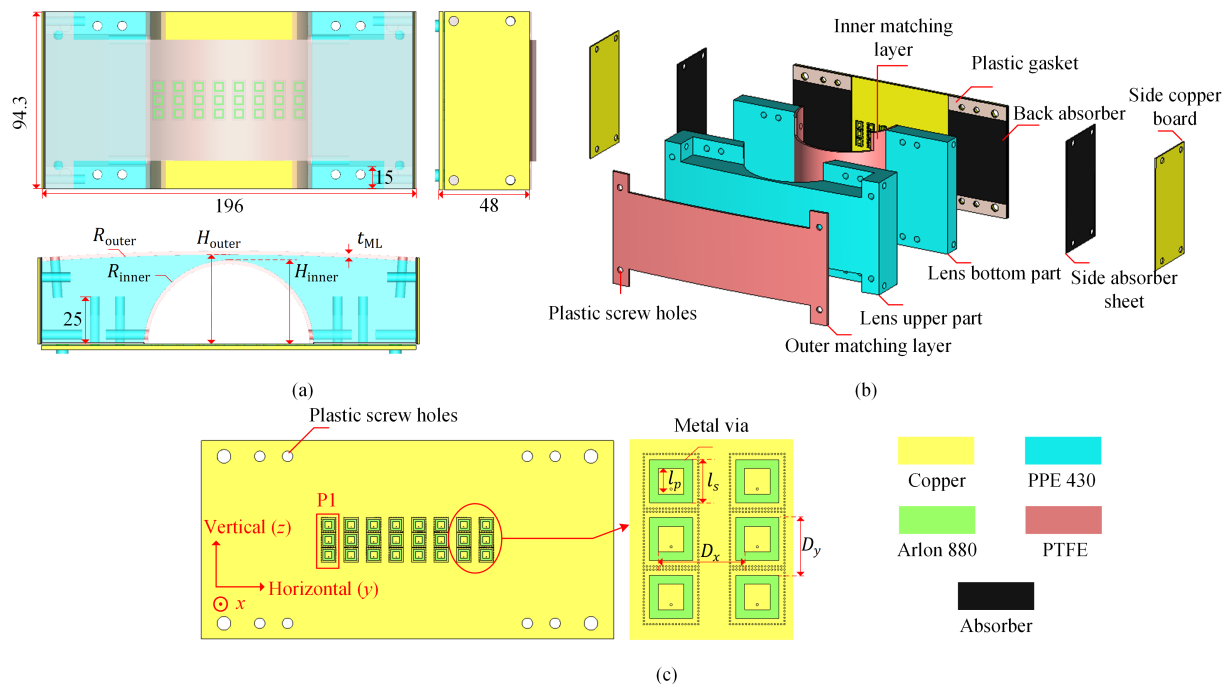


Fig. 12. (a) Perspective and (b) structural view of the array with DDL. (c) Illustration of the 3×8 patch array. $H_{inner} = 43.91$, $R_{inner} = 44.38$, $H_{outer} = 46.78$, $R_{outer} = 1370.2$, $t_{ML} = 2$, $l_p = 3.18$, $l_s = 5.36$, $D_x = 10.71$, and $D_y = 7.18$ (units: mm).

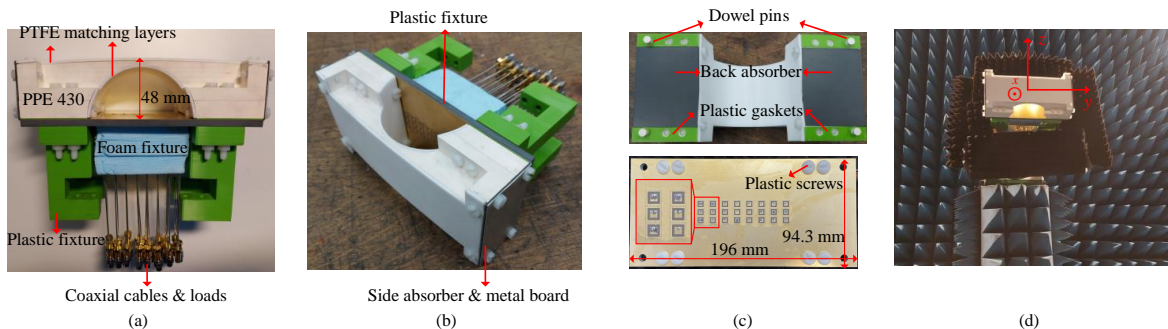


Fig. 13. Manufactured uniform under-sampled array with DDL: (a) top view, (b) side view, (c) bottom view of the DDL and top view of the patch array, and (d) array with DDL under measurement.

C. Scanning Performance of Array with DDL

An agreement can also be found between simulated and measured synthesized radiation patterns of the antenna array, as shown in Fig. 15(a) - (c). For the MDB, compared to the standalone array, DDL increases its beam width on the H-plane and, in contrast, narrows its beam width on the E-plane, as summarized in Table. I. The beam width variation can also be found in the simulated 3-D synthesized array radiation patterns scanning to different directions ϕ_{MDB} , as shown in Fig. 16. Since the same DDL is responsible for both deflecting the MDB and reducing grating lobes, a trade-off is evident: on the H-plane, the beam width of the MDB is enlarged, which limits the ability to achieve a narrow beam with high gain.

Moreover, in Fig. 15(a) - (b), as the MDB scans from 0° to 60° , the standalone array exhibits strong grating lobes with a realized gain ranging from 5 to 21 dBi within the range of $\phi \subseteq [270^\circ, 360^\circ)$. However, these grating lobes are

TABLE I
COMPARISON OF ARRAY'S 3-DB BEAMWIDTH AT 28 GHZ

Array	ϕ_{MDB} (deg)				
	0	15	30	45	60
Standalone (H-plane)	6.3	6.5	7.2	8.8	12.2
wi DDL (H-plane)	15.2	16.3	16.5	19.5	23.3
Standalone (E-plane)	25.3	25.3	25.3	24.3	23.5
wi DDL (E-plane)	14.9	17.2	19.5	20.2	21.8

significantly reduced to below 5 dBi with the help of the DDL. In addition, as the MDB scans to different angles, Fig. 17 illustrates the simulated excitation phase differences ($\Delta\beta$) between horizontally adjacent antennas. This indicates that the excitation phase distribution is linear for the standalone array, while it is non-linear for the array integrated with DDL due to the non-uniform insertion phases introduced by the curved DDL.

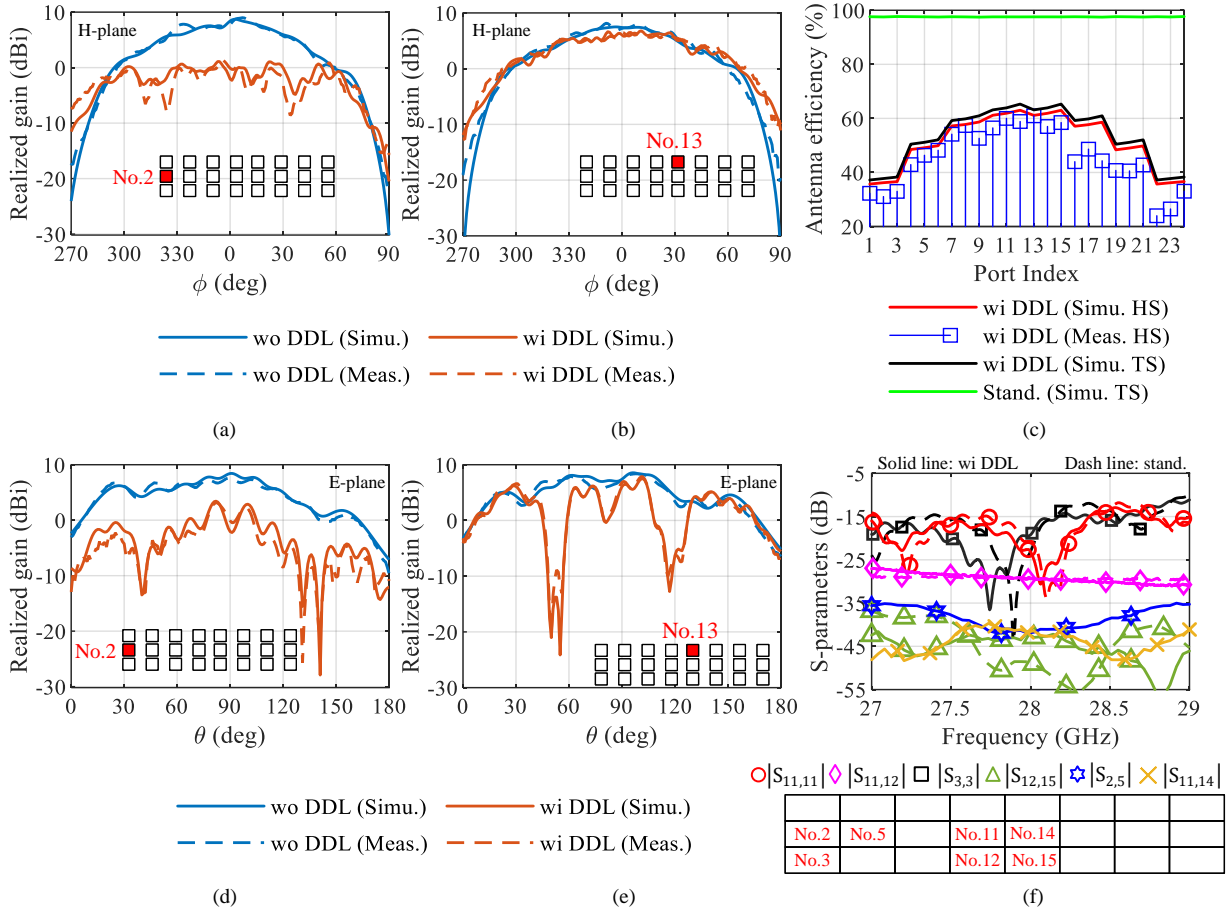


Fig. 14. Simulated and measured embedded radiation patterns at 28 GHz for element No.2 (a, d) and element No.13 (b, e) in the standalone array and the array with DDL, on the H plane ($\theta = 90^\circ$) (a, b) and the E plane ($\phi = 0^\circ$) (d, e). (c) Simulated and measured antenna efficiencies for half sphere (HS) and total sphere (TS). (f) Measured reflection coefficients and mutual coupling between certain elements.

Fig. 18(a) compares the simulated and measured scanning performance at 28 GHz between the standalone array and the array with DDL. In the scan range of $\phi_{\text{MDB}} = 0^\circ$ to $\phi_{\text{MDB}} = 60^\circ$, the standalone array has a maximum SL of over 7 dB. Moreover, as the MDB scans from $\phi_{\text{MDB}} = 0^\circ$ to $\phi_{\text{MDB}} = 60^\circ$, the gain of the strongest side-lobe continues to increase, even surpassing the MDB in the range of $\phi_{\text{MDB}} \subseteq [30^\circ, 60^\circ]$, resulting in a negative SLL. However, the integration of the DDL keeps the gain of the strongest side-lobe consistently lower than that of the MDB, resulting in an SLL of at least 9 dB over a scan range from 0° to about 55° . Furthermore, although the DDL enlarges the beam width and consequently decreases the MDB gain, it significantly reduces the maximum SL from 7 dB to 3 dB. Overall, the integration of the DDL allows the under-sampled array, which has one-wavelength inter-element spacing, to achieve effective beam scanning performance.

Additionally, it is important to note that the DDL has been constructed in a cylindrical shape to simplify design and fabrication while prioritizing scanning performance, particularly the SL and SLL in the horizontal plane, as discussed throughout this paper. However, there is still potential for future work to enhance the gain of the MDB through more

detailed design, which may include vertically curving the DDL. This modification aims to eliminate the splits observed in the E-plane radiation patterns of the antennas (as illustrated in Fig. 14(d)-(e)) and to align the radiation from the antenna elements in the same column, thereby achieving maximum combined beam gain on the H-plane (*xy* plane).

D. Discussions on Radiation Efficiency, Frequency Bandwidth Performance, and Active Reflection Coefficient

As expected from the efficiency of antenna elements in the array shown in Fig. 14(c), the array with DDL has lower radiation efficiency (RE) than the standalone array when scanning, as summarized in Table II. However, the grating lobes of the standalone array should be avoided for the radio service, motivating to evaluate the MDB radiation efficiency (MDBRE) instead of the RE. The MDBRE is the power efficiency within a cone region around the MDB axis, determined by the required beam width θ_{MDBRE} , as illustrated in Fig. 19 and represented as

$$\text{MDBRE} = \frac{1}{4\pi} \int_0^{2\pi} \int_0^{\theta_{\text{MDBRE}}} G(\theta', \phi') \sin \theta' d\theta' d\phi', \quad (11)$$

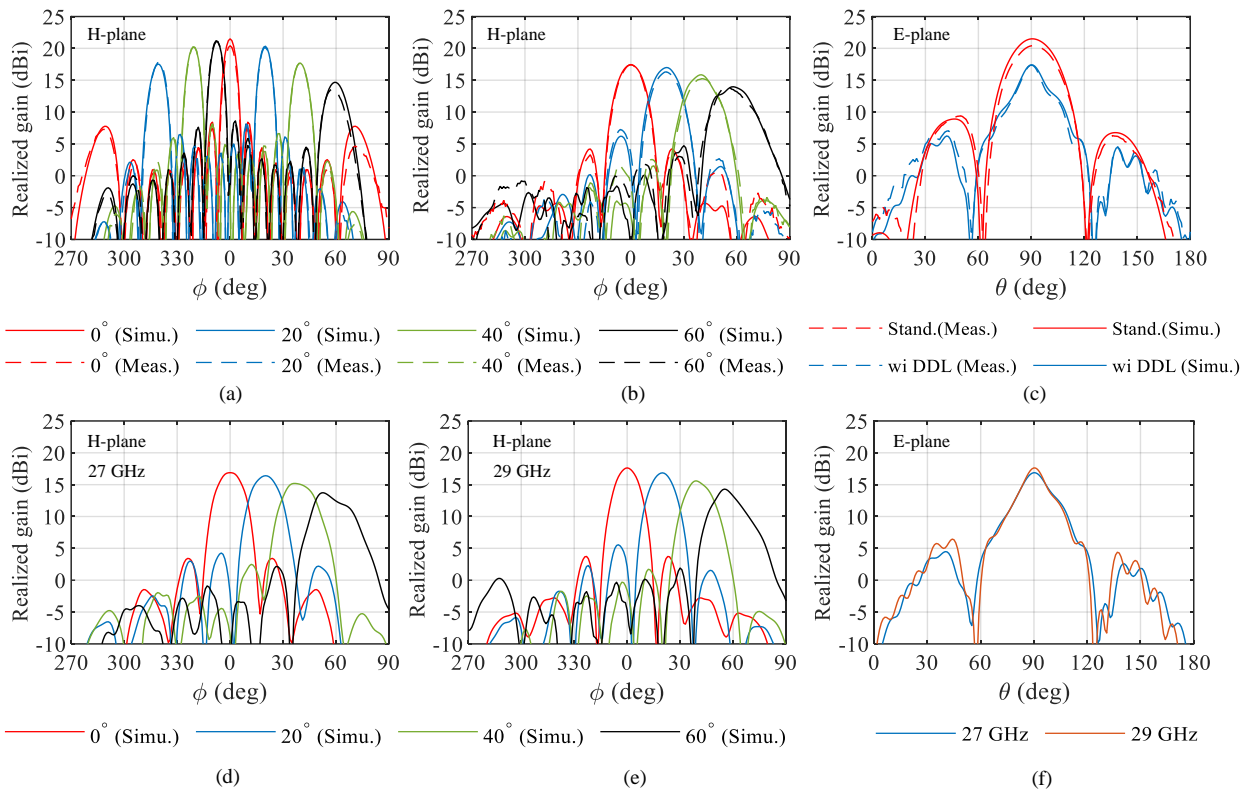


Fig. 15. Simulated and measured scanning patterns on H-plane of (a) standalone array, (b) array with DDL, and (c) a comparison on E-plane at 28 GHz. Simulated scanning patterns (d) - (f) of the array with DDL at 27 and 29 GHz.

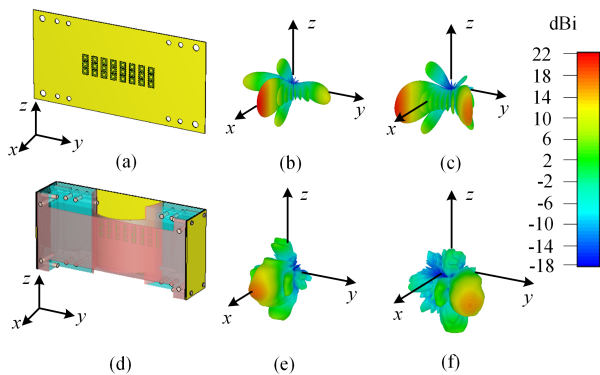


Fig. 16. Simulated 3-D synthesized array's gain patterns at 28 GHz for (a) standalone array when (b) $\phi_{MDB} = 0^\circ$ and (c) $\phi_{MDB} = 45^\circ$, and (d) array with DDL when (e) $\phi_{MDB} = 0^\circ$ and (f) $\phi_{MDB} = 45^\circ$.

where $G(\theta', \phi')$ is the gain pattern (linear form) of the array. It should be noted that the integration in (11) is based on the local coordinate system $x'y'z'$ defined by the target direction, as shown in Fig. 19. The MDBRE indicates the efficiency of the power conveyed to the target direction without considering the grating lobe. Since the scanning performance on the xoy plane (H-plane) is mainly considered, it is reasonable that θ_{MDBRE} on the $x'o'z'$ plane determines the integration region of the MDBRE in (11). Therefore, for different values of ϕ_{MDB} , and considering a certain service beam width on the xoy plane (θ_{MDBRE} determined by Th as shown in Fig. 19),

the simulated MDBREs of both the standalone array and the array with DDL for $Th = 3$ and 6 dB are summarized in Table II. The integration of the DDL increases the power portion of the MDB relative to the total radiation power of the array during scanning. Although some variations in the beam width caused by the DDL contribute to the improvement of the MDBRE, the similarity in MDBRE values before and after DDL integration indicates that the observed reduction in the radiation efficiency of the array and antennas, as shown in Table II and Fig. 14(c), primarily occurs in directions that are not considered, including those corresponding to grating lobes. This finding also highlights the effectiveness of the DDL in reducing the radio interference caused by the grating lobe while enabling effective beam scanning in an under-sampled array.

In addition, the substantial horizontal inter-element spacing of the array results in low mutual couplings, as illustrated in Fig. 14(f). This characteristic contributes to consistently low active reflection coefficients, which remain below -15 dB during scanning, as shown in Fig. 20. Furthermore, as shown in Figs. 15(d) - (f) and Fig. 18(b), the scanning performance of the array with DDL designed at a point frequency at 28 GHz also maintains at 27 and 29 GHz, making it applicable to systems with a certain bandwidth. Additionally, when the MDB is oriented at $\phi_{MDB} = 60^\circ$, the array operating at 27 GHz exhibits a smaller electrical aperture size compared to that operating at 29 GHz, resulting in a wider beamwidth with distortion, as shown in Fig. 15(d) - (e) [24].

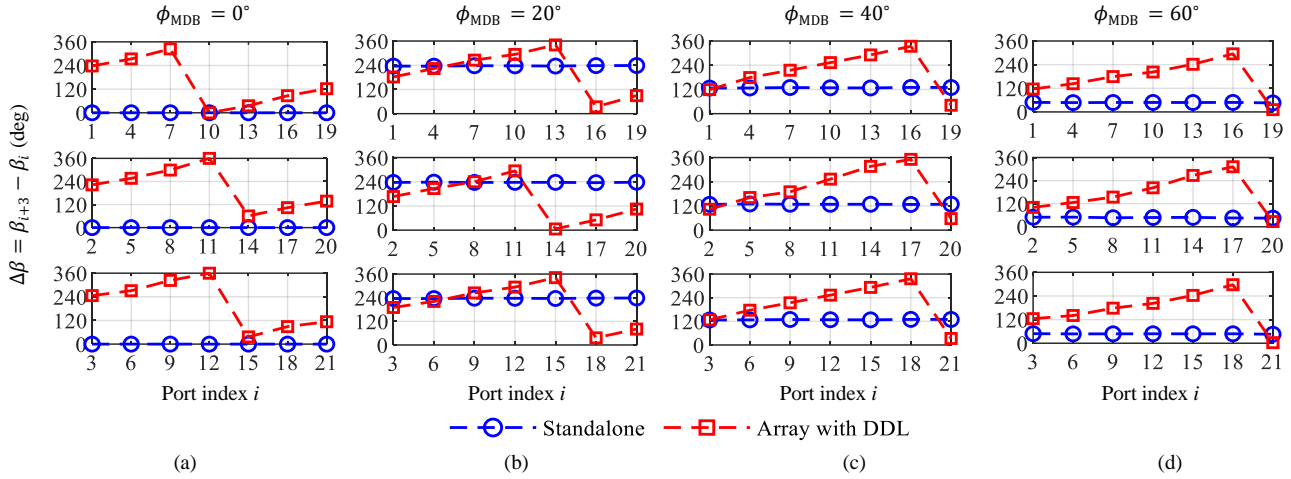


Fig. 17. Simulated excitation phase differences ($\Delta\beta$) between adjacent antenna elements in the same row, i.e., ports i and $i + 3$, for the 3×8 standalone array and the array with DDL, shown for (a) $\phi_{\text{MDB}} = 0^\circ$, (b) 20° , (c) 40° , and (d) 60° .

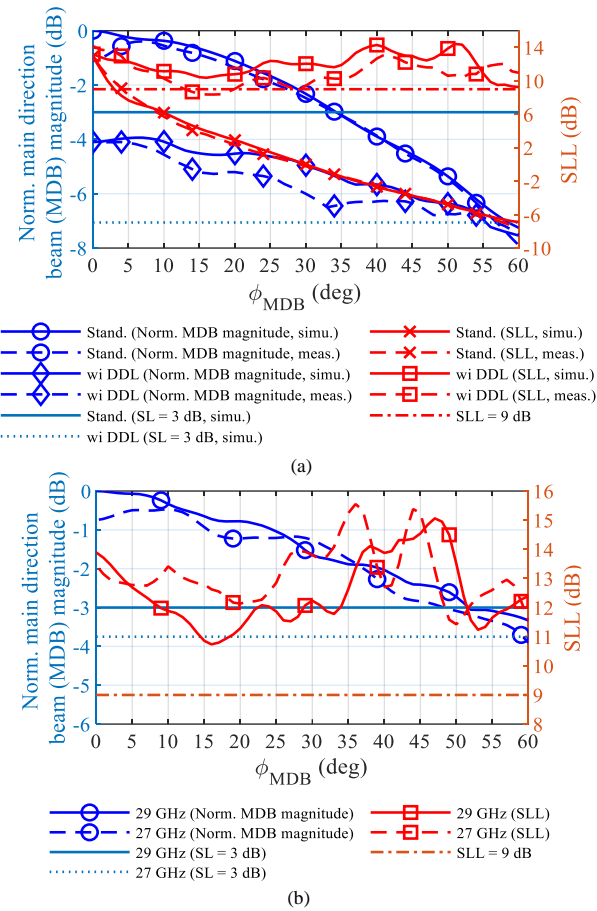


Fig. 18. (a) Simulated and measured normalized MDB magnitude and SLL for the standalone array and the array with DDL, respectively. (b) Simulated normalized MDB magnitude and SLL for the array with DDL at 27 and 29 GHz, respectively.

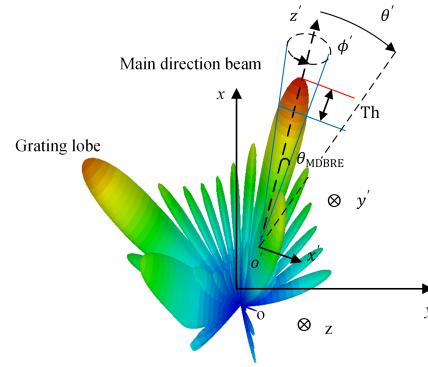


Fig. 19. Illustration of evaluating the main direction beam radiation efficiency (MDBRE). The z' and y' are parallel to the main direction beam axis and z -axis, respectively. θ' starts from the positive z' within $[0^\circ, 180^\circ]$, and ϕ' starts from the positive x' within $[0^\circ, 360^\circ]$.

TABLE II
SIMULATED RADIATION EFFICIENCY (RE) AND MAIN DIRECTION BEAM RADIATION EFFICIENCY (MDBRE) OF THE ARRAY FOR DIFFERENT SCAN ANGLES AT 28 GHz

Efficiency (%)	ϕ_{MDB} (deg)				
	0	15	30	45	60
RE (stand.)	98.29	98.47	98.63	98.58	98.94
RE (wi DDL)	60.26	59.35	56.38	49.72	42.92
MDBRE (Th = 3 dB, stand.)	8.75	7.61	6.05	6.11	8.71
MDBRE (Th = 3 dB, wi DDL)	17.14	17.04	15.00	19.47	11.90
MDBRE (Th = 6 dB, stand.)	14.24	12.89	11.11	10.73	14.82
MDBRE (Th = 6 dB, wi DDL)	24.95	25.63	24.88	28.03	21.08

In summary, for an under-sampled array with one-wavelength inter-element spacing, grating lobes are unavoidable and can sometimes be stronger than the MDB. As a

result, such configurations are unsuitable for beam scanning in communication systems. Although the implementation of the

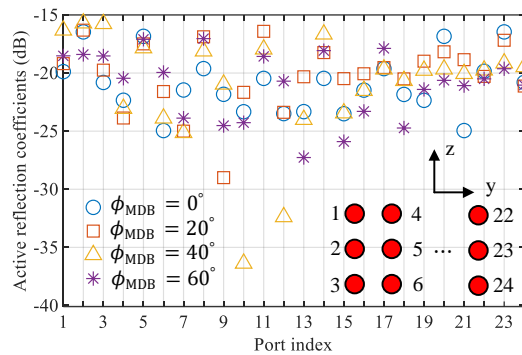


Fig. 20. Simulated active reflection coefficients of the array with DDL for different scan angles at 28 GHz.

DDL increases the beamwidth of the MDB and decreases its gain, several advantages are achieved:

1) The implementation of the DDL enables the under-sampled array to achieve a symmetrical-to-boresight continuous beam-scanning range of 110° , while maintaining the SL below 3 dB and ensuring that the strongest side lobes remain consistently more than 9 dB lower than the MDB.

2) The under-sampled array equipped with DDL exhibits measured coupling below -35 dB, which is significantly lower than the coupling observed in arrays with an inter-element spacing of half a wavelength, typically around -15 dB [41] [42] [43]. This measured coupling also lower than the -25 dB threshold required for massive MIMO arrays in industrial applications [43]. Furthermore, the active reflection coefficients of the under-sampled array with DDL consistently remain below -15 dB during scanning, demonstrating superior performance compared to the compact array with DDL, which reports several active reflection coefficients exceeding -10 dB within the H-plane scan range of $[45^\circ, 60^\circ]$ at 22 GHz [24]. Low mutual coupling renders the under-sampled array with DDL suitable for use as a phased array, MIMO array, and hybrid analog/digital array, in which the number of digital chains is fewer than the number of antennas [41].

3) The under-sampled array with large inter-element spacing exhibits lower heat density compared to one with half-wavelength spacing. Characterized by reduced grating lobes and effective beam scanning performance due to the implementation of the DDL, under-sampled array would significantly alleviate the challenge of managing heat dissipation from surrounding active RF components in an integrated front-end design.

VII. CONCLUSION

This article presents an effective design for the DDL, enabling the under-sampled array, with an inter-element spacing of one wavelength, to achieve beam scanning with reduced grating lobes. By utilizing the GO algorithm and an optimization process, the DDL shape is initially determined based on the required scanning performance, chosen material, and dimensional limitations. The performance of the DDL is then evaluated for different materials and profiles, demonstrating

that a DDL with higher permittivity and a larger profile can achieve a broader scanning region.

Moreover, the full-wave simulation reveals that the total reflection induced by the DDL plays an important role in reducing the grating lobe. This finding helps to make the DDL from theory to practise, including methods such as DDL miniaturization and the implementation of the absorber sheets and matching layers. Subsequent optimization based on the full-wave simulation is conducted to address factors ignored by the GO algorithm and to account for structural changes in the DDL.

Finally, a rectangular patch array equipped with a DDL working at 28 GHz is fabricated and measured to demonstrate the effectiveness of this method. The implementation of the DDL enables the under-sampled array, with an inter-element spacing of λ , to achieve a symmetrical-to-boresight continuous beam-scanning range of 110° , while maintaining the SL below 3 dB and ensuring that the strongest side lobes remain consistently more than 9 dB lower than the MDB. This scanning performance is effective within a bandwidth of 2 GHz. Additionally, the under-sampled array equipped with DDL exhibits measured coupling below -35 dB and active reflection coefficients below -15 dB.

Since total reflection is theoretically independent of the grating lobe's polarization and the DDL design method uses a simplified model with periodic boundaries, this suggests that the DDL design has the potential to enable two-dimensional beam scanning with reduced grating lobes based on rotational symmetry, applicable to an uniform, under-sampled square planar array. The under-sampled array, characterized by reduced grating lobes and effective beam scanning performance, would significantly alleviate the challenge of managing heat dissipation from surrounding active RF components in an integrated front-end design, making it suitable for millimeter-wave communication systems.

ACKNOWLEDGMENT

The authors would like to thank Antti Kuhlberg and Matti Vaaja at the School of Electrical Engineering, Aalto University, for their help with the array and DDL manufacture and test.

REFERENCES

- [1] F.-L. Jin, X. Ding, Y.-F. Cheng, B.-Z. Wang, and W. Shao, "A wideband phased array with broad scanning range and wide-angle impedance matching," *IEEE Transactions on Antennas and Propagation*, vol. 68, no. 8, pp. 6022–6031, 2020.
- [2] F.-L. Jin, W. Shao, L.-Y. Xiao, B.-Z. Wang, and B. Jiang, "Substrate-integrated cavity-backed array with controlled mutual coupling for wide scanning," *IEEE Antennas and Wireless Propagation Letters*, vol. 21, no. 4, pp. 808–812, 2022.
- [3] C.-H. Hu, B.-Z. Wang, G.-F. Gao, R. Wang, S.-Q. Xiao, and X. Ding, "Conjugate impedance matching method for wideband and wide-angle impedance matching layer with 70° scanning in the h-plane," *IEEE Antennas and Wireless Propagation Letters*, vol. 20, no. 1, pp. 63–67, 2021.
- [4] Y. Wang, X. Chen, X. Liu, J. Yi, J. Chen, A. Zhang, and A. A. Kishk, "Improvement of diversity and capacity of mimo system using scatterer array," *IEEE Transactions on Antennas and Propagation*, vol. 70, no. 1, pp. 789–794, 2021.
- [5] M. Li, X. Chen, A. Zhang, A. A. Kishk, and W. Fan, "Reducing correlation in compact arrays by adjusting near-field phase distribution for mimo applications," *IEEE Transactions on Vehicular Technology*, vol. 70, no. 8, pp. 7885–7896, 2021.

- [6] C. A. Balanis, *Antenna theory: analysis and design*. John Wiley & sons, 2016.
- [7] Z. Ding, J. Chen, H. Liu, C. He, and R. Jin, "Grating lobe suppression of sparse phased array by null scanning antenna," *IEEE Transactions on Antennas and Propagation*, vol. 70, no. 1, pp. 317–329, 2021.
- [8] Y. Mu, J. Han, D. Xia, H. Liu, and L. Li, "A self-decoupling wide-angle scanning pattern reconfigurable antenna array using parasitic comb structures," *IEEE Transactions on Antennas and Propagation*, pp. 1–1, 2024.
- [9] Q. Ren, B. Qian, X. Chen, X. Huang, Q. Li, J. Zhang, and A. A. Kishk, "Linear antenna array with large element spacing for wide-angle beam scanning with suppressed grating lobes," *IEEE Antennas and Wireless Propagation Letters*, vol. 21, no. 6, pp. 1258–1262, 2022.
- [10] Z. Iqbal and M. Pour, "Exploiting higher order modes for grating lobe reduction in scanning phased array antennas," *IEEE Transactions on Antennas and Propagation*, vol. 67, no. 11, pp. 7144–7149, 2019.
- [11] Z. Ding, J. Chen, H. Zhou, and R. Jin, "Two-dimensional scanning phased array with large element spacing using pattern reconfigurable stacked patch antenna at ka-band," *IEEE Transactions on Antennas and Propagation*, vol. 70, no. 7, pp. 5447–5457, 2022.
- [12] Y. Mu, J. Han, D. Xia, H. Liu, and L. Li, "A self-decoupling wide-angle scanning pattern reconfigurable antenna array using parasitic comb structures," *IEEE Transactions on Antennas and Propagation*, vol. 72, no. 2, pp. 1212–1223, 2024.
- [13] P. Chakravorty and D. Mandal, "Grating lobe suppression with discrete dipole element antenna arrays," *IEEE Antennas and Wireless Propagation Letters*, vol. 15, pp. 1234–1237, 2015.
- [14] Y. Zeng, X. Ding, Y. Wang, W. Shao, and B.-Z. Wang, "A square-rate arrangement method for large-spacing planar phased array grating lobes homogenization," *IEEE Transactions on Antennas and Propagation*, vol. 70, no. 9, pp. 7538–7545, 2022.
- [15] P. Rocca, R. J. Mailloux, and G. Toso, "Ga-based optimization of irregular subarray layouts for wideband phased arrays design," *IEEE Antennas and Wireless Propagation Letters*, vol. 14, pp. 131–134, 2015.
- [16] W. Zhang, L. Li, and F. Li, "Reducing the number of elements in linear and planar antenna arrays with sparseness constrained optimization," *IEEE Transactions on Antennas and Propagation*, vol. 59, no. 8, pp. 3106–3111, 2011.
- [17] C. Bencivenni, M. Ivashina, R. Maaskant, and J. Wettergren, "Design of maximally sparse antenna arrays in the presence of mutual coupling," *IEEE Antennas and Wireless Propagation Letters*, vol. 14, pp. 159–162, 2014.
- [18] X. Xu, C. Liao, L. Zhou, and F. Peng, "Grating lobe suppression of non-uniform arrays based on position gradient and sigmoid function," *IEEE Access*, vol. 7, pp. 106407–106416, 2019.
- [19] D. Pinchera, M. D. Migliore, M. Lucido, F. Schettino, and G. Panariello, "Efficient large sparse arrays synthesis by means of smooth re-weighted l1 minimization," *Electronics*, vol. 8, no. 1, p. 83, 2019.
- [20] A. Salmi, J. Bergman, A. Lehtovuori, J. Ala-Laurinaho, and V. Viikari, "Grating-lobe mitigation using parasitic scatterers and principal component analysis," *IEEE Transactions on Antennas and Propagation*, vol. 72, no. 2, pp. 1995–2000, 2024.
- [21] Y. Kerzhner and A. Epstein, "Metagrating-assisted high-directivity sparse regular antenna arrays for scanning applications," *IEEE Transactions on Antennas and Propagation*, vol. 71, no. 1, pp. 650–659, 2022.
- [22] H. Wang, S.-W. Qu, and S. Yang, "Grating lobe suppression of large element spacing array by angle selective surface," *IEEE Antennas and Wireless Propagation Letters*, vol. 23, no. 7, pp. 2180–2184, 2024.
- [23] A. Benini, E. Martini, S. Monni, M. C. Viganò, F. Silvestri, E. Gandini, G. Gerini, G. Toso, and S. Maci, "Phase-gradient meta-dome for increasing grating-lobe-free scan range in phased arrays," *IEEE Transactions on Antennas and Propagation*, vol. 66, no. 8, pp. 3973–3982, 2018.
- [24] L. Xiao, S.-W. Qu, and S. Yang, "3-d printed dielectric dome array antenna with $\pm 80^\circ$ beam steering coverage," *IEEE Transactions on Antennas and Propagation*, vol. 70, no. 11, pp. 10494–10503, 2022.
- [25] A. Algaba-Brazález, H. Wang, P. Castillo-Tapia, L. Manholm, M. Johansson, and O. Quevedo-Teruel, "Flexible 6g antenna systems based on innovative lenses combined with array antennas," in *2023 17th European Conference on Antennas and Propagation (EuCAP)*. IEEE, 2023, pp. 1–5.
- [26] E. Gandini, F. Silvestri, A. Benini, G. Gerini, E. Martini, S. Maci, M. C. Viganò, G. Toso, and S. Monni, "A dielectric dome antenna with reduced profile and wide scanning capability," *IEEE Transactions on Antennas and Propagation*, vol. 69, no. 2, pp. 747–759, 2021.
- [27] M. Pubill-Font, F. Mesa, A. Algaba-Brazález, S. Clendinning, M. Johansson, and O. Quevedo-Teruel, "2d ray tracing model for multilayer dielectric dome arrays with inner reflections," *IEEE Open Journal of Antennas and Propagation*, pp. 1–1, 2024.
- [28] Y.-H. Lv, X. Ding, B.-Z. Wang, and D. E. Anagnostou, "Scanning range expansion of planar phased arrays using metasurfaces," *IEEE Transactions on Antennas and Propagation*, vol. 68, no. 3, pp. 1402–1410, 2020.
- [29] M. Durach, F. Williamson, J. Adams, T. Holtz, P. Bhatt, R. Moreno, and F. Smith, "On fresnel-airy equations, fabry-perot resonances and surface electromagnetic waves in arbitrary bianisotropic metamaterials, including with multi-hyperbolic fresnel wave surfaces," *Progress In Electromagnetics Research*, vol. 173, pp. 53–69, 2022.
- [30] H. Steyskal, A. Hessel, and J. Shmoy, "On the gain-versus-scan trade-offs and the phase gradient synthesis for a cylindrical dome antenna," *IEEE Transactions on Antennas and Propagation*, vol. 27, no. 6, pp. 825–831, 1979.
- [31] A. Rebollo, Á. F. Vaquero, M. Arrebola, and M. R. Pino, "3d-printed dual-reflector antenna with self-supported dielectric subreflector," *IEEE Access*, vol. 8, pp. 209091–209100, 2020.
- [32] A. Corporation., "Preperm™ low loss dielectric thermoplastics," 2023. [Online]. Available: <https://www.avient.com/products/engineered-polymer-formulations/conductive-signal-radiation-shielding-formulations/preperm-low-loss-dielectric-thermoplastics>
- [33] G. Deschamps, "Ray techniques in electromagnetics," *Proceedings of the IEEE*, vol. 60, no. 9, pp. 1022–1035, 1972.
- [34] S.-W. Lee, M. S. Sheshadri, V. Jamnejad, and R. Mittra, "Refraction at a curved dielectric interface: geometrical optics solution," *IEEE Transactions on Microwave Theory and Techniques*, vol. 30, no. 1, pp. 12–19, 1982.
- [35] J. A. Kong, "Theory of electromagnetic waves," *New York*, 1975.
- [36] T. M. Inc., "Surrogate optimization algorithm," Natick, Massachusetts, United States, 2024. [Online]. Available: <https://www.mathworks.com/help/gads/surrogate-optimization.html>
- [37] B. Ahn, I.-J. Hwang, K.-S. Kim, S.-C. Chae, J.-W. Yu, and H. L. Lee, "Wide-angle scanning phased array antenna using high gain pattern reconfigurable antenna elements," *Scientific Reports*, vol. 9, no. 1, p. 18391, Dec 2019. [Online]. Available: <https://doi.org/10.1038/s41598-019-54120-2>
- [38] Y. Wang, X. Huang, J. Zhao, Z. Zhong, W. E. Sha, and X. Chen, "Experimental investigation of scatterer-array-based decorrelation technique applied to real multiple-input multiple-output base station," *Electronics Letters*, vol. 59, no. 8, p. e12796, 2023. [Online]. Available: <https://ietresearch.onlinelibrary.wiley.com/doi/abs/10.1049/ell2.12796>
- [39] T. M. Inc., "Parallel computing toolbox," Natick, Massachusetts, United States, 2024. [Online]. Available: <https://www.mathworks.com/help/parallel-computing/>
- [40] A. Microwave., "10.2ghz-28ghz high frequency radio absorbing material," 2023. [Online]. Available: <https://www.atlanticmicrowave.com/catalogue/cables-assemblies-and-accessories/102ghz-28ghz-high-frequency-radio-absorbing-material>
- [41] X. Chen, H. Pei, M. Li, H. Huang, Q. Ren, Q. Wu, A. Zhang, and A. A. Kishk, "Revisit to mutual coupling effects on multi-antenna systems," *Journal of Communications and Information Networks*, vol. 5, no. 4, pp. 411–422, 2020.
- [42] K.-L. Wu, C. Wei, X. Mei, and Z.-Y. Zhang, "Array-antenna decoupling surface," *IEEE Transactions on Antennas and Propagation*, vol. 65, no. 12, pp. 6728–6738, 2017.
- [43] S. Zhang, X. Chen, and G. F. Pedersen, "Mutual coupling suppression with decoupling ground for massive mimo antenna arrays," *IEEE Transactions on Vehicular Technology*, vol. 68, no. 8, pp. 7273–7282, 2019.



Yipeng Wang received the B.S. and M.S. degrees from Northwestern Polytechnical University in Xi'an, China, in 2015 and 2018, respectively. He is currently pursuing a Ph.D. in the School of Information and Communication Engineering at Xi'an Jiaotong University, Xi'an, China. From November 2022 to November 2023, he served as a visiting doctoral researcher in the School of Electrical Engineering at Aalto University, Espoo, Finland. His research interests include the design of MIMO and phased array antennas.



Katsuyuki Haneda (Member, IEEE) is an Associate Professor with the School of Electrical Engineering, Aalto University, Espoo, Finland. His current research activity covers high-frequency radios such as millimeter-waves and beyond and wireless for medical and smart-city applications. Dr. Haneda was the author and coauthor of several best paper and student paper awards at the IEEE Vehicular Technology Conference and European Conference on Antennas and Propagation, among others. He received the R. W. P. King Paper Award from IEEE

Transactions on Antennas and Propagation in 2021, together with Dr. Usman Virk. He was the Technical Program Committee Co-Chair of the 17th European Conference on Antennas and Propagation (EuCAP 2023), Florence, Italy. He was an Associate Editor of IEEE Transactions on Antennas and Propagation from 2012 to 2016 and an Editor of IEEE Transactions on Wireless Communications from 2013 to 2018. He was the Guest Editor of Special Issues on IEEE Antennas and Propagation Aspects of In-Band Full-Duplex Applications and IEEE Artificial Intelligence in Radio Propagation for Communications from IEEE Transactions on Antennas and Propagation in 2021 and 2022, respectively.



Clemens Icheln received the Dipl.-Ing. degree in electrical engineering from the Harburg University of Technology, Hamburg, Germany, in 1996, and the Licentiate and D.Sc. Tech. degrees in radio engineering from Aalto University, Espoo, Finland, in 1999 and 2001, respectively. He is currently a Senior University Lecturer with the Department of Electronics and Nanoengineering, School of Electrical Engineering, Aalto University. His current research interests include the design of multielement antennas for small communication devices such as mobile

terminals and medical implants, to operate at frequency ranges as low as 400 MHz but also up to mm-wave frequencies, as well as the development of suitable antenna characterization methods that allow taking, for example, the effects of the radio channel into account.



Juha Ala-Laurinaho received the Dip.Eng. (M.Sc.) degree in mathematics and D.Sc. (Tech.) degree in electrical engineering from the TKK Helsinki University of Technology, Espoo, Finland, in 1995 and 2001, respectively. He has been with Aalto University, formerly TKK, serving with Radio Laboratory, from 1995 to 2007, with the Department of Radio Science and Engineering, from 2008 to 2016, and at present with the Department of Electronics and Nanoengineering. He is currently working as a Staff Scientist. He has been a Researcher and Project

Manager in various millimeter-wave technology-related projects. His current research interests include antennas and antenna measurement techniques for millimeter and submillimeter waves, and millimeter wave imaging.



Juha Tuomela received the B.S. degree in electrical engineering from the School of Electrical Engineering, Aalto University, Espoo, Finland, in 2023. He is currently pursuing the M.S. degree in microwave engineering with Aalto University. His research interests include channel sounding, antenna design, and antenna measurements.



Lauri Vähä-Savo (Member, IEEE) received the B.E. and M.E. degrees from the Aalto University School of Electrical Engineering, Espoo, Finland, in 2016 and 2019, respectively. He is currently pursuing the D.Sc. degree with the Department of Electronics and Nanosciences within the Antennas and Propagation Group, Aalto University, Espoo. He is currently working in the field of 5G antennas and outdoor-to-indoor communication. His research interests include a microwave and millimeter-wave antenna design, human antenna interaction, and smart

buildings and cities.



Bing Xue (Graduate Student Member, IEEE) was born in Henan, China. He is currently pursuing the D.Sc. (Tech.) degree in radio engineering with the School of Electrical Engineering, Aalto University, Espoo, Finland. His current research interests include antenna designs and measurements, human-antenna interaction simulation and measurements, and electromagnetic modeling focusing on mm-wave frequencies for 5G systems and beyond.



Xiaoming Chen (Senior Member, IEEE) received the B.Sc. degree in electrical engineering from Northwestern Polytechnical University, Xi'an, China, in 2006, and M.Sc. and Ph.D. degrees in electrical engineering from Chalmers University of Technology, Gothenburg, Sweden, in 2007 and 2012, respectively. From 2013 to 2014, he was a postdoctoral researcher at the same University. From 2014 to 2017, he was with Qamcom Research & Technology AB, Gothenburg, Sweden. Since 2017, he has been a professor at Xi'an Jiaotong University, Xi'an, China.

His research areas include MIMO antennas, over-the-air testing, reverberation chambers, and Electromagnetic information theory. He has published more than 220 journal articles on these topics. Prof. Chen currently serves as a Track Editor for IEEE Antennas and Wireless Propagation Letters, and an Associate Editor for IEEE Transactions on Antennas and Propagation. He was the general chair of the IEEE International Conference on Electronic Information and Communication Technology (ICEICT) in 2021. He received the IEEE outstanding Associate/Track Editor awards seven times, 2018-2024, and URSI (International Union of Radio Science) Young Scientist Award 2017 and 2018.